Applied Surface Science 706 (2025) 163590

Contents lists available at ScienceDirect

Applied Surface Science

journal homepage: www.elsevier.com/locate/apsusc

Full Length Article

Formation of 3D-$Cr_2(C_{1-y}O_y)$ at Cr_2AlC / AlO_x interfaces

Rajib Sahu [a,b,1,2,*], Peter J. Pöllmann [b,2,**], Dimitri Bogdanovski [b], Clio Azina [b], Ganesh Kumar Nayak [b], Jochen M. Schneider [a,b], Christina Scheu [a,c,*]

[a] Max-Planck-Institut für Eisenforschung GmbH, Max-Planck-Str. 1, 40237 Düsseldorf, Germany
[b] Materials Chemistry, RWTH Aachen University, Kopernikusstr. 10, 52074 Aachen, Germany
[c] Materials Analytics, RWTH Aachen University, Kopernikusstr. 10, 52074 Aachen, Germany

ARTICLE INFO

Keywords:
Interface
MAX phase
3D-$Cr_2(C_{1-y}O_y)$
C defect
iDPC STEM
DFT

ABSTRACT

We report on the microstructural characterization of a multilayer AlO_x-Cr_2AlC thin film grown at 580 °C by direct current magnetron sputtering. Instead of stabilizing a two-dimensional carbide derivative, intentional periodic excess oxygen incorporation during thin film deposition leads to the formation of a 3D-$Cr_2(C_{1-y}O_y)$ phase within the AlO_x-Cr_2AlC multilayered film. The microstructure of the film was investigated by combining various imaging techniques in aberration corrected scanning transition electron microscopy. The distribution of C and related defects at atomic scale was revealed by the integrated differential phase contrast method.

1. Introduction

Two-dimensional (2D) transition metal borides (MBenes) or carbides (MXenes) exhibit great potential for application in sustainable energy technologies [1–4]. Due to their distinctive features – such as large surface area, excellent mechanical and thermal stability, as well as metallic conductivity – they are promising candidates for various energy-related applications, including battery electrodes, electrocatalysis, photocatalysis, and energy storage systems [2–6]. Typically, precursor materials such as transition metal aluminium boride (MAB) and transition metal aluminium carbide (MAX) phases are synthesized at temperatures exceeding 1000 °C [7,8]. Subsequent aluminium deintercalation, often achieved by chemical etching with concentrated acidic or alkaline solutions, leads to the formation of their 2D derivatives; termed MBenes and MXenes, respectively [9,10]. However, the drawbacks of high synthesis temperatures for precursor materials, along with concerns related to toxicity, laboratory safety, as well as health issues associated with handling etching agents, and the extended deintercalation time of partial aluminium etching, present challenges in both 2D MBenes and MXene production [11,12]. Moreover, the stability of 2D MBenes and MXenes in the solution phase is often questioned, as various compositional defect phases form simultaneously. For instance, stabilizing a Cr_2C MXene from the Cr_2AlC MAX phase through chemical etching poses a formidable challenge [13] due to bulk and anisotropic chromium carbides being favored over the 2D Cr_2C MXene phase during chemical etching [14,15]. Cr-based MXenes are challenging to synthesize [15,16] as they show low synthesizability scores [17] compared to other transition metal carbides, predicted by machine learning model. Theoretical studies predict 2D Cr_2C MXene as a superior material in various applications, such as electrocatalysis for hydrogen evolution reaction (HER) [18–21], hydrogen storage [22], oxygen evolution reaction (OER) [19,21], and lithium and non-lithium-ion batteries [23–25]. The proposed significance of Al-deintercalated Cr_2AlC MAX phase requires a new synthesis approach. An alternative and straightforward method has been established for synthesizing 2D MoB MBene from the parental precursor MoAlB MAB phase, without the need for chemical etching [26,27]. This method can be executed at a lower synthesis temperature compared to bulk synthesis using a thin film approach [28,29]. In this approach, Al deintercalation occurs due to the presence of residual oxygen during thin film deposition, resulting in the formation of a MoAlB-2D MoB MBene-AlO_x heterostructure at grain boundaries [26,27]. This approach effectively reduces the cost and time needed for high-temperature and chemical etching processes, which are problematic for industrial applications and pose safety concerns.

In this work, we report on the formation of 3D $Cr_2(C_{1-y}O_y)$ phase at AlO_x-Cr_2AlC interfaces in a multilayered thin film synthesized by

* Corresponding authors at: Max-Planck-Institut für Eisenforschung GmbH, Max-Planck-Str. 1, 40237 Düsseldorf, Germany.
** Corresponding author.
E-mail addresses: rajib.sahu@kit.edu (R. Sahu), poellmann@mch.rwth-aachen.de (P.J. Pöllmann), c.scheu@mpie.de (C. Scheu).
[1] Now at: Institute of Nanotechnology, Karlsruhe Institute of Technology, Hermann-von-Helmholtz-Platz 1, 76344 Eggenstein-Leopoldshafen, Germany.
[2] These authors contributed equally to the manuscript.

https://doi.org/10.1016/j.apsusc.2025.163590
Received 7 March 2025; Received in revised form 16 May 2025; Accepted 20 May 2025
Available online 20 May 2025

intentional periodic oxygen incorporation at 580 °C using physical vapor deposition. A detailed analysis utilizing various imaging techniques in advanced scanning transmission electron microscopy (STEM) was performed. The atomic position of C column in both Cr_2AlC and $Cr_2(C_{1-y}O_y)$ phases was determined by integrated differential phase contrast (iDPC) STEM imaging. The projected interatomic bond distances of $Cr_2(C_{1-y}O_y)$ phase were in good agreement with theoretical distances obtained from density functional theory (DFT) calculations. As this 3D $Cr_2(C_{1-y}O_y)$ phase has not been observed previously, its functional properties and potential applications are yet to be explored.

2. Experimental Methods

Multilayer AlO_x-Cr_2AlC thin films were deposited by direct current (DC) magnetron sputtering (DCMS) in a laboratory-scale high-vacuum deposition chamber using a single ternary 2″ compound Cr_2AlC target (Plansee Composite Materials GmbH, Germany) operated at 200 W. 10x10x0.5 mm^3 single crystalline MgO (100) (Crystal GmbH, Germany) were used as substrates and kept at floating potential. The target-to-substrate distance was 10 cm and the target was facing the substrate. The base pressure at the deposition temperature of 580 °C was $< 2.30 \times 10^{-6}$ mbar. Sputtering was conducted at an Ar (99.999 % purity) pressure of 0.50 Pa. To deposit multilayer thin films, after each 6 min of pure Ar deposition, oxygen was periodically introduced for 2 min during the deposition. The overall deposition time was 1 h leading to a film thickness of ~ 1.6 μm as shown by electron microscopy.

3. Transmission electron microscopy

A probe corrected ThermoFisher Titan Themis was operated at an acceleration voltage of 300 kV for conducting STEM investigations. Microstructural characterizations were initially carried out using a focused ion beam (FIB) lift-out TEM sample, which was prepared using a Thermo Fisher Scientific dual beam Scios 2 HiVac system. In addition, cross-sectional and plan-view TEM samples were prepared and thinned down below 20 nm by conventional mechanical polishing and Ar ion milling in a Gatan PIPS. A convergence angle of 23.8 mrad was chosen for high resolution STEM. Collection angles ranging from 10–16 mrad and 78–200 mrad were used for annular bright field (ABF) and high angle annular dark field (HAADF) imaging, respectively. During iDPC STEM, the collection angle was adjusted to 10–53 mrad. The microscope is equipped with a Bruker SuperX detector for energy-dispersive X-ray spectroscopy (EDX) analysis. Energy electron loss spectroscopy (EELS) was performed at 1 eV energy resolution measured from full width at half maximum (FWHM) of the zero-loss peak. Selected area electron diffraction (SAED) experiment was done with an image corrected ThermoFisher Titan Themis.

4. Density functional theory

Density functional theory calculations were used to estimate and compare the bond lengths with the measured ones. The initial structural model of $Cr_2(CO)$ was constructed by substituting O in place of Al in a Cr_2AlC MAX phase structure obtained from literature [30]. The calculations were carried out using the Vienna Ab initio Simulation Package (VASP) [31,32] and the generalized gradient approximation with Perdew-Burke-Ernzerhof [33] parametrization for the electron–electron exchange and correlation interactions. The used pseudo-potentials for each element, i.e., Cr, O, C, treat semi-core states as valence such as Cr_pv: $3p^6 3d^5 4s^1$, O: $2s^2 2p^4$, C: $2s^2 2p^2$. The ion–electron interactions were described using the projector augmented wave method [34], with a plane-wave cut-off of 500 eV. The corresponding Brillouin zone was sampled with a 13 × 13 × 3 Monkhorst-Pack k-point mesh [35]. The Methfessel-Paxton [36] smearing of 0.15 eV was applied. A convergence criterion of 10^{-6} eV (per supercell) was used for the total energy during the electronic self-consistency cycles. The total energy convergence of 10^{-5} eV (per supercell) was applied for ionic relaxations during structural optimizations. The cells were relaxed regarding size, shape, and atomic positions. Since Cr_2AlC is antiferromagnetic in the ground state [37], the calculations for $Cr_2(CO)$ were considered with the spin-polarized antiferromagnetic with the initial magnetic moments 3.0, 1.0, 0.5 for Cr, O, C, respectively. Though the resultant magnetic moment was zero after optimization, the antiferromagnetic calculation is in the ground state compared to ferromagnetic and non-magnetic calculations, as revealed by the total energy, see Table 1.

5. Results and discussion

The microstructure of the synthesized AlO_x-Cr_2AlC multilayer thin film is readily visible in the representative HAADF STEM micrograph shown in Fig. 1(a). White arrows highlight the repeating amorphous AlO_x layers in the film, formed during synthesis due to the introduction of oxygen. In low magnification HAADF STEM images, Cr_2AlC and AlO_x can be distinguished by Z (atomic number) contrast: the bright regions are Cr-rich while the dark grey areas are Al rich, given that the intensity is roughly proportional to Z^2 [38]. Pores with a size of ~ 30–70 nm (marked by yellow arrows) appear throughout the film in the interface regions, and additional investigations covering small to large pores are provided in the supplementary material (fig. S1). It is reasonable to assume that the pore formation observed in the MAX phase layer is caused by Al deintercalation, which in turn results in both the formation of 3D-$Cr_2(C_{1-y}O_y)$ as well as Al vacancy clustering. Fig. 1(b) shows a higher magnification of a section of the film where Cr_2AlC and $Cr_2(C_{1-y}O_y)$ phases are differentiated. Selected area electron diffraction (SAED) and fast Fourier transformations (FFTs) confirm the presence of Cr_2AlC MAX phase with lattice parameters $a = 2.8 \pm 0.1$ Å and $c = 13 \pm 0.1$ Å in accordance with previously reported values from our group [39–41]. A detailed structure parameter analysis is available in the supplementary material (fig. S2).

The $Cr_2(C_{1-y}O_y)$ grains exhibit a relatively brighter appearance, indicated by red arrows in the HAADF STEM image, compared to the MAX phase. The Cr_2AlC regions show characteristics of columnar growth, with the grains grown perpendicular to the substrate surface. The average length and width of the grains are ranging from 150 to 250 nm and 40 to 150 nm, respectively. A similar measurement was carried out for $Cr_2(C_{1-y}O_y)$ grains with their length and width varying between 10 to 50 nm and 5 to 40 nm, respectively. The areal fraction of $Cr_2(C_{1-y}O_y)$ regions compared to the Cr_2AlC MAX phase is <15 %. The supplementary material (fig. S1-S2) includes a representative grain size measurement to provide a statistical analysis of the formation of both Cr_2AlC and $Cr_2(C_{1-y}O_y)$ domains in terms of average size and distribution. X-ray diffraction (XRD) data are presented in supplementary Fig. S3. Due to low volume fraction of the $Cr_2(C_{1-y}O_y)$ phase, no indication of its phase formation can be inferred from the XRD data.

The chemical composition of the film was measured on a representative section of the film (Fig. 1(a)) and the corresponding EDX maps of the constituting elements (Cr, Al, C, and O) are shown in Fig. 1(c)-(f) along with substrate constituent Mg (Fig. 1(g)). It is evident from the STEM EDX maps that Cr and C are mostly constrained to the Cr_2AlC layers and uniformly distributed therein while Al and O are distributed over the whole film thickness with their highest concentration in the AlO_x layers (Fig. 1(c)-(f)). Interestingly, the Al concentration at the

Table 1
Estimated total energy and formation energy of 3D Cr_2AlC, 3D Cr_2OC, and 2D Cr_2OC in their preferential magnetic states from density functional theory calculations.

System	Preferable Magnetic state	Total energy (eV/atom)	E_f (eV/atom)
Cr_2AlC	Antiferro	−8.1853	−0.100
3D Cr_2OC	Antiferro	−8.9680	−0.714
2D Cr_2OC	Ferro	−8.6150	−0.361

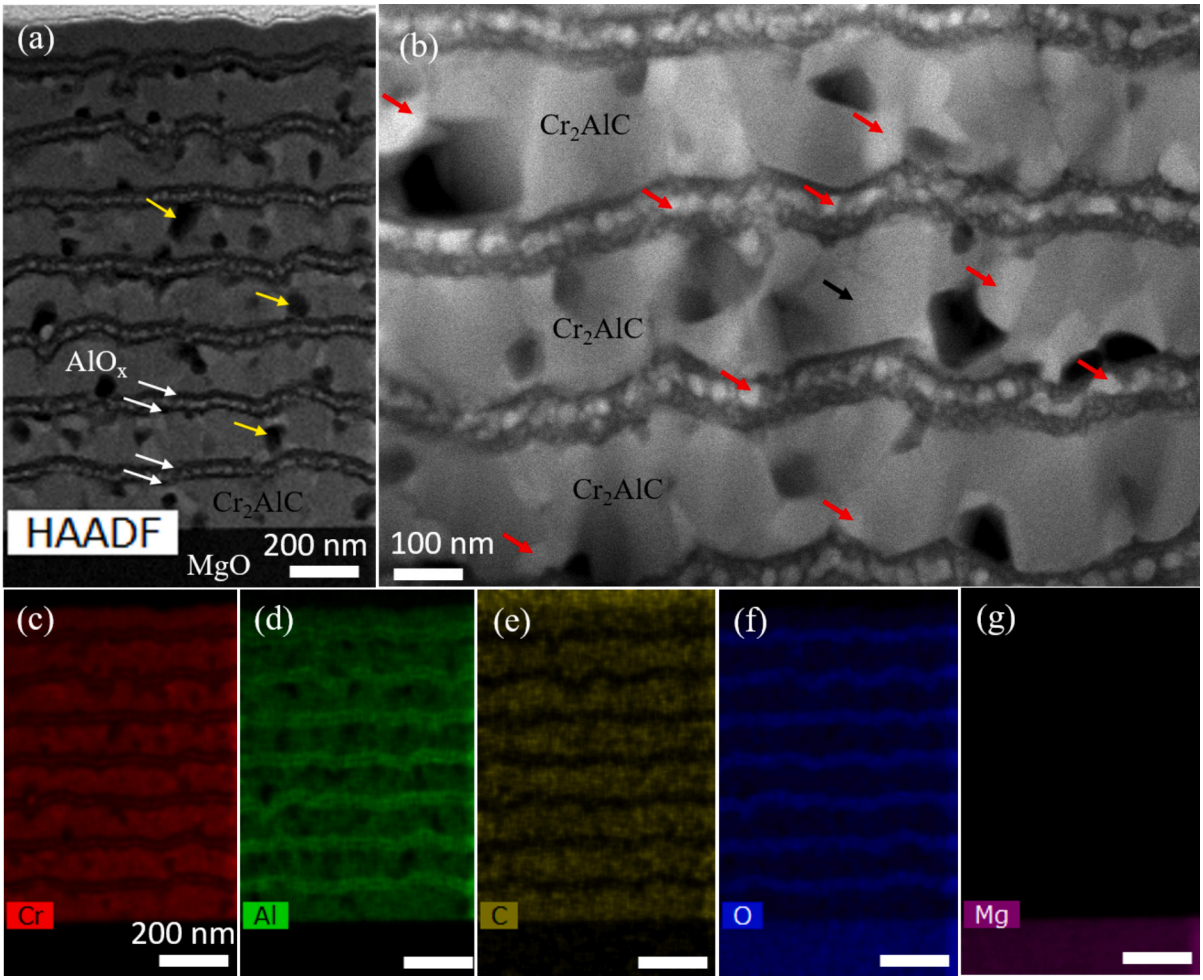

Fig. 1. (a) Overview of AlO_x-Cr_2AlC multilayer thin film in cross-sectional HAADF STEM image. White arrows identify AlO_x. Pores are marked by representative yellow arrows. (b) HAADF STEM micrograph distinguishing grains of Cr_2AlC MAX and oxygen containing $Cr_2(C_{1-y}O_y)$ phases by red arrows. (c)-(g) present elemental STEM EDX mapping of Cr, Al, C, O, and Mg of the region shown in (a).

interfaces to the MAX phase is higher compared to the center region of AlO_x regions, while small traces of Cr seem to be only present in that center region. The preferential Al distribution indicates a selective removal of Al from the Cr_2AlC structure into the AlO_x layers. This can be rationalized based on the MAX phase bonding state: the metallic M−A bonds within the MAX phase are significantly weaker compared to the covalent/ionic M−X bonds, rendering Al the most weakly bound species and, hence, facilitating its removal [15]. The EDX maps shown in Fig. 1 (c)-(g), a clear separation of Cr_2AlC and AlO_x layers can be seen, while $Cr_2(C_{1-y}O_y)$ cannot be identified conclusively. Since O K_α (0.525 keV) and Cr L_α (0.573 keV) lines have a similar characteristic X-ray energy range, accurate chemical quantification by STEM EDX is challenging. Therefore, STEM EELS has been carried out to analyze the relative atomic composition of Cr_2AlC and $Cr_2(C_{1-y}O_y)$ phases. The elemental EELS analysis involves five measurements over $Cr_2(C_{1-y}O_y)$ grains, yielding an approximate composition of Cr: 60 ± 1.79 at%, C: 32.2 ± 1.67 at%, and O: 8.06 ± 1.05 at%. A similar statistical mean average measurement over Cr_2AlC grains revealed their composition to be ~ Cr: 50.44 ± 3.63 at%, Al: 22.46 ± 1.25 at%, C: 24.8 ± 1.06 at%, and O: 2.3 ± 1 at%.

Fig. 2 shows a more detailed microscopic characterization of the AlO_x-Cr_2AlC multilayer film. The existence of the $Cr_2(C_{1-y}O_y)$ phase is evident from the Z contrast in the low magnification HAADF STEM image (Fig. 2 (a)) as the regions appear brighter compared to the Cr_2AlC regions. Therefore, concurrent phase formation of Cr_2AlC along with $Cr_2(C_{1-y}O_y)$ at the grain boundary is observed. Fig. 2(b) shows a high resolution (HR) HAADF STEM image of the region marked by the white dotted rectangle in Fig. 2(a). A representative ideal structural overlay (Cr, Al, and C atomic columns marked here and throughout this work by red, green, and orange dots, respectively) is given for the easier distinction of individual phases. Due to Z contrast, Cr columns appear brighter, while Al columns exhibit a dark grey contrast. Caused by its low scattering amplitude, the light element C is invisible in the micrograph. A FFT shown in the top left inset of Fig. 2(b), confirms the synthesis of hexagonal Cr_2AlC MAX phase along the [10–10] zone axis (ZA), while the structure of the 3D $Cr_2(C_{1-y}O_y)$ crystal is revealed by the FFT inset given in the bottom right corner. The lattice parameter 'c' of this phase is measured to be around 4.6 ± 0.1Å and is in very good agreement with our DFT-calculated value of 4.75Å. The slight difference of ~ 3 % might result from the calculations being performed at 0 K and in thermodynamic equilibrium, while the samples were synthesized at high temperature and under kinetically limited conditions.

It is evident from Fig. 2 that concurrent phase formation of Cr_2AlC and 3D-$Cr_2(C_{1-y}O_y)$ occurs at the grain boundaries in the vicinity of AlO_x regions. This is accompanied by a significant decrease of the Al concentration within the matrix in proximity to the AlO_x layers. Hence, the formation of 3D-$Cr_2(C_{1-y}O_y)$ phase is indicated to be caused by incorporated oxygen, facilitating the out-diffusion of Al from the Cr_2AlC grains, and in turn leading to the formation of amorphous AlO_x at the grain boundaries. The STEM EDX line scan across a grain boundary, shown in Fig. 2(h)-(i), reveals an Al concentration profile consistent with our proposed mechanism in which Al out-diffusion drives the formation

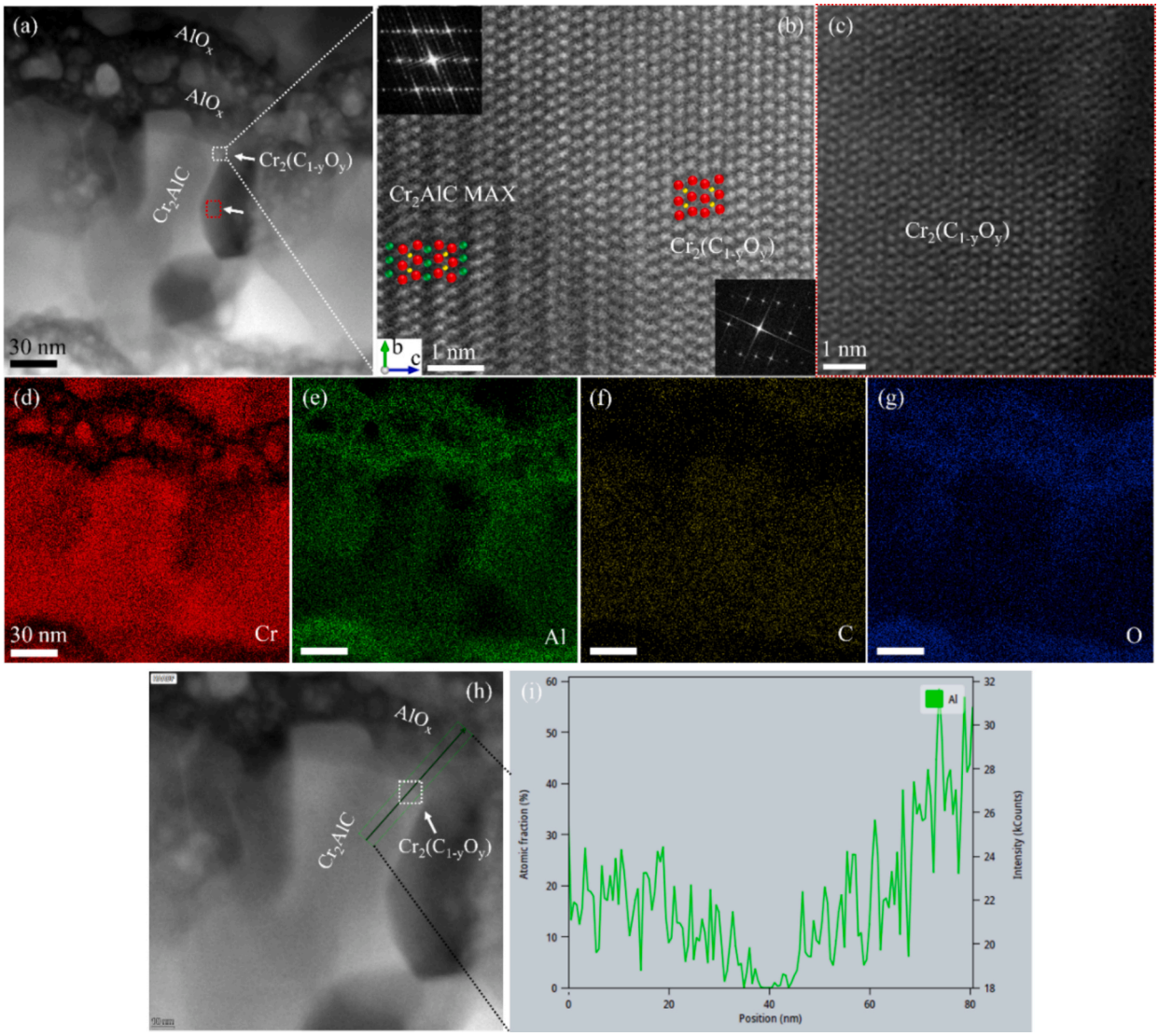

Fig. 2. (a) HAADF STEM image of AlO_x-Cr_2AlC grain with $Cr_2(C_{1-y}O_y)$ phase. The interface of the Cr_2AlC-$Cr_2(C_{1-y}O_y)$ heterostructure is shown in a higher magnification in the HRSTEM image in (b). Here and throughout the text, red, green, and orange coloured dots represent Cr, Al, and C atomic columns in the ideal structural overlays, respectively. (c) HRSTEM micrograph of $Cr_2(C_{1-y}O_y)$ phase in the vicinity of a pore in the region marked by a red rectangle in (a). (d)-(g) present EDX maps of Cr, Al, C, and O recorded of the region shown in (a). (i) STEM EDX line profile shows the Al concentration variation across the $Cr_2AlC - Cr_2(C_{1-y}O_y) - AlO_x$ regions (h).

of the 3D-$Cr_2(C_{1-y}O_y)$ phase. This observation aligns with our earlier studies on the synthesis of 2D MoB MBene in a MoAlB MAB phase thin film, where residual oxygen gas induced Al deintercalation and formation of amorphous AlO_x regions at grain boundaries [26,27]. While a 2D MoB MBene structure within the transition metal boride (MoAlB MAB phase) was observed, the transition metal carbide (Cr_2AlC MAX phase) results in the formation of a 3D-Cr_2C phase containing additional oxygen. This is in line with literature report stating that bulk and anisotropic chromium carbides are being favored over the 2D Cr_2C MXene phase during chemical etching [14]. Fig. 2(c) shows a high magnification image of the region marked by a red dotted rectangle in Fig. 2(a). Here, additional formation of $Cr_2(C_{1-y}O_y)$ near a pore is observed. However, the exact role of pore formation for the occurrence of oxygen containing $Cr_2(C_{1-y}O_y)$ phase needs to be investigated further. More images showing similar areas are available in the supplementary material (fig. S4). Elemental STEM EDX maps from the region in Fig. 2(a) are shown in Fig. 2(d)-(g) to further support these findings.

Fig. 3(a) shows a plan view HAADF STEM micrograph of a $Cr_2(C_{1-y}O_y)$ grain along the [001] orientation. Other phases including Cr_2AlC MAX, amorphous AlO_x, and pores are marked in the image, their presence being indicated by the different Z contrast. A chemical analysis by STEM EDX mapping provides further indication for the coexistence of these various phases in the supplementary material (fig. S5). HRSTEM characterization of the 3D-$Cr_2(C_{1-y}O_y)$ phase of the area within the white dotted rectangle in Fig. 3(a), located in the vicinity of a grain boundary, is shown in Fig. 3(b). The white arrow indicates the direction of increased crystal thickness, causing an increase in intensity (as shown in the supplementary material fig. S6) from the grain boundary towards the center of the grain. The FFT inset in Fig. 3(b) confirms the hexagonal structural characteristic of the 3D-$Cr_2(C_{1-y}O_y)$ phase along the [001] ZA. A higher magnification HAADF HRSTEM image from the region marked with the white rectangle in Fig. 3(b) is shown in Fig. 3(c). It can be readily seen that a honeycomb structure is formed by the Cr atomic columns, with C atoms most likely occupying the center of the hexagon. The C atoms are not visible here due to their low scattering amplitude. The lattice parameters 'a' and 'b' were measured to be $\sim 3 \pm 0.1$ Å and are therefore in excellent agreement with the DFT-predicted value of 3 Å. For the identification of the light element C, simultaneous

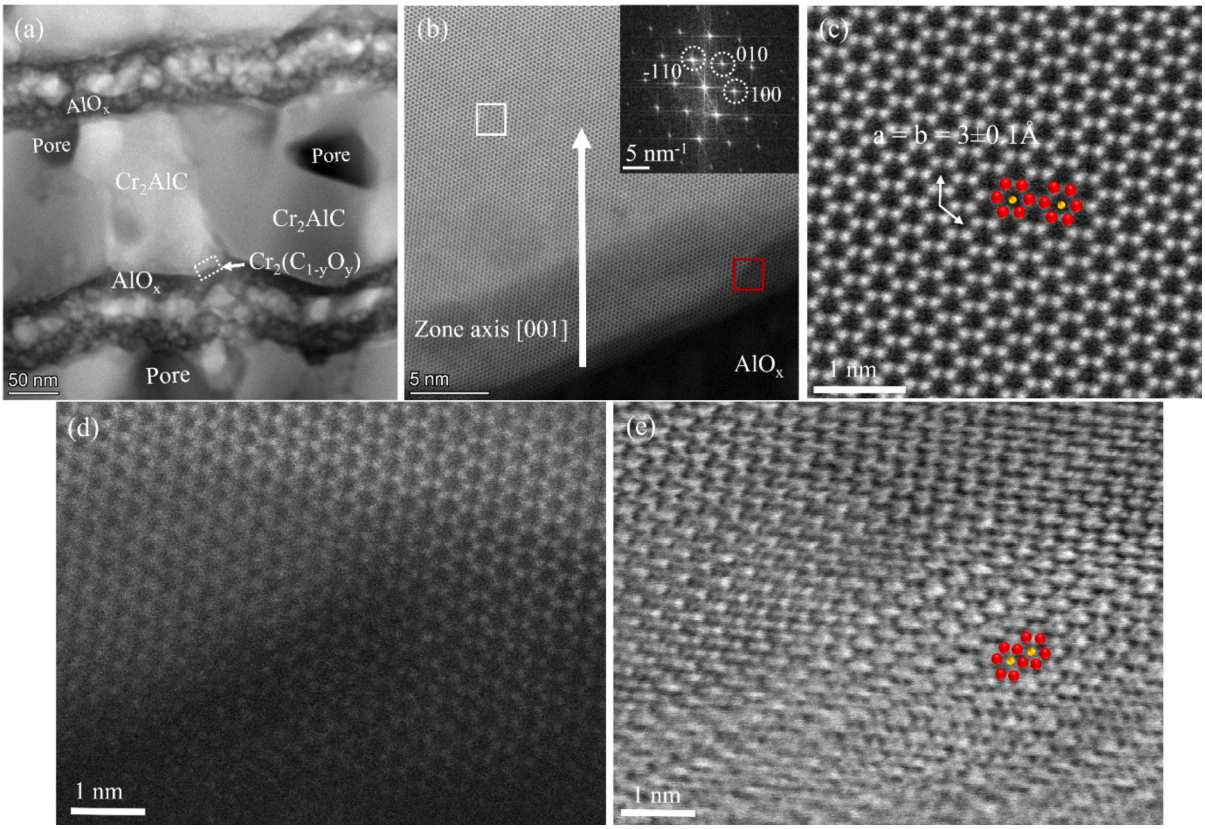

Fig. 3. A grain of $Cr_2(C_{1-y}O_y)$ is identified along the [001] ZA (a). The region marked with a white dotted rectangle at the grain boundary is analyzed in (b)-(e). HAADF STEM shows increasing crystal thickness along the direction of the white arrow (b). The FFT inset reveals a hexagonal crystal structure of Cr_2C. An HRSTEM image acquired from white rectangle shows a hexagonal honeycomb structure of Cr_2C phase (c). Correlating HAADF (d) and ABF STEM (e) images are compared to identify the atomic structure of C within the Cr_2C phase.

acquisition of HAADF (Fig. 3(d)) and ABF STEM (Fig. 3(e)) of the region marked with the red rectangle in Fig. 3(b) were performed. ABF STEM, a well-recognized method used for imaging light elements, where the intensity is proportional to $Z^{1/3}$ [42], reveals C atoms as a faint white contrast and Cr columns as bright regions in Fig. 3(e). A projected experimental Cr-C bond distance of 1.75 ± 0.1 Å was measured from this region, aligning well with the $Cr_2(C_{1-y}O_y)$ system simulated by DFT calculations, for which a bond distance of 1.73 Å is predicted.

To precisely locate the position of C columns in both Cr_2AlC and $Cr_2(C_{1-y}O_y)$ phases, simultaneous acquisition of HAADF and iDPC STEM were performed along with EELS measurements (Fig. 4(a)-(d)). A HAADF STEM image of the Cr_2AlC MAX phase along the [10–10] ZA is shown in Fig. 4(a)) and the corresponding iDPC STEM micrograph is presented in Fig. 4(b). Fig. 4(c) depicts a HRSTEM image of the $Cr_2(C_{1-y}O_y)$ phase along the [100] ZA and its corresponding iDPC STEM image (Fig. 4(d)) reveals the positions of the Cr and C atomic columns. Changes in the image contrast for the C columns are identified by white arrows in the iDPC STEM micrographs (Fig. 4(b) and (d)). This could be due to missing atomic columns of C in both Cr_2AlC and $Cr_2(C_{1-y}O_y)$ phases. The identification of such C defects serves to confirm the theoretical predictions made by DFT calculations [43]. To Baben et al. have demonstrated that, unlike Ti_2AlC and V_2AlC MAX phases, the formation of a C vacancy requires a minimal energy of 0.9 eV in the Cr_2AlC MAX phase [43]. Moreover, the calculations propose that oxygen incorporation can partly substitute the carbon atomic column within the lattice. A comparative STEM EELS measurement was performed to distinguish the chemical and fine electronic structures of Cr_2AlC and $Cr_2(C_{1-y}O_y)$ phases (Fig. 4(e)). The O K edge at 532.6 eV shows an oxygen content of around 8.06 ± 1.05 at% within the $Cr_2(C_{1-y}O_y)$ phase. By correlating iDPC, STEM EELS, and DFT calculations, it is indicated that incorporated oxygen may either replace some of the C columns or occupy the vacancies in the atomic column of carbon [42].

The magnetron sputtering technique has proven effective in synthesizing a 2D MoB MBene within a $MoAlB/AlO_x$ heterostructure film [26,27], while yielding a 3D-$Cr_2(C_{1-y}O_y)$ phase in a multilayer Cr_2AlC/AlO_x film. Our analysis suggests that the emergence of the 3D-$Cr_2(C_{1-y}O_y)$ phase is likely caused by the selective out-diffusion of aluminium from the Cr_2AlC MAX phase grain. The diffusion is facilitated by the oxygen incorporation during the synthesis process, resulting in the formation of AlO_x regions at the grain boundaries. The formation of the 3D-$Cr_2(C_{1-y}O_y)$ phase is thereby favored over the formation of the 2D MXene derivative. This is consistent with the comparison of the predicted energy of formation of 3D-$Cr_2(CO)$ with the competing 2D variant and the MAX phase Cr_2AlC (Table 1), which clearly indicates that the energetically most stable configuration is 3D-$Cr_2(CO)$. The negative energy of formation of 0.1 eV/atom for Cr_2AlC is consistent with the here reported formation of Cr_2AlC as no oxygen is present / incorporated, while – in presence of oxygen – the experimentally observed formation of the 3D-$Cr_2(C_{1-y}O_y)$ phase vs the 2D-$Cr_2(C_{1-y}O_y)$ is again consistent with the more negative energy of formation for the 3D variant compared to the 2D variant. Hence, the here observed formation of 3D-$Cr_2(C_{1-y}O_y)$ phase can be rationalize based on DFT predictions. Exploring magnetic domains at Cr_2AlC-$Cr_2(C_{1-y}O_y)$ grain boundaries using a combination of DPC STEM and DFT presents an intriguing direction for future research.

6. Conclusion

In summary, we present a comprehensive microstructural characterization of an AlO_x-Cr_2AlC multilayered thin film synthesized by magnetron sputtering. Formation of a 3D-$Cr_2(C_{1-y}O_y)$ as well as

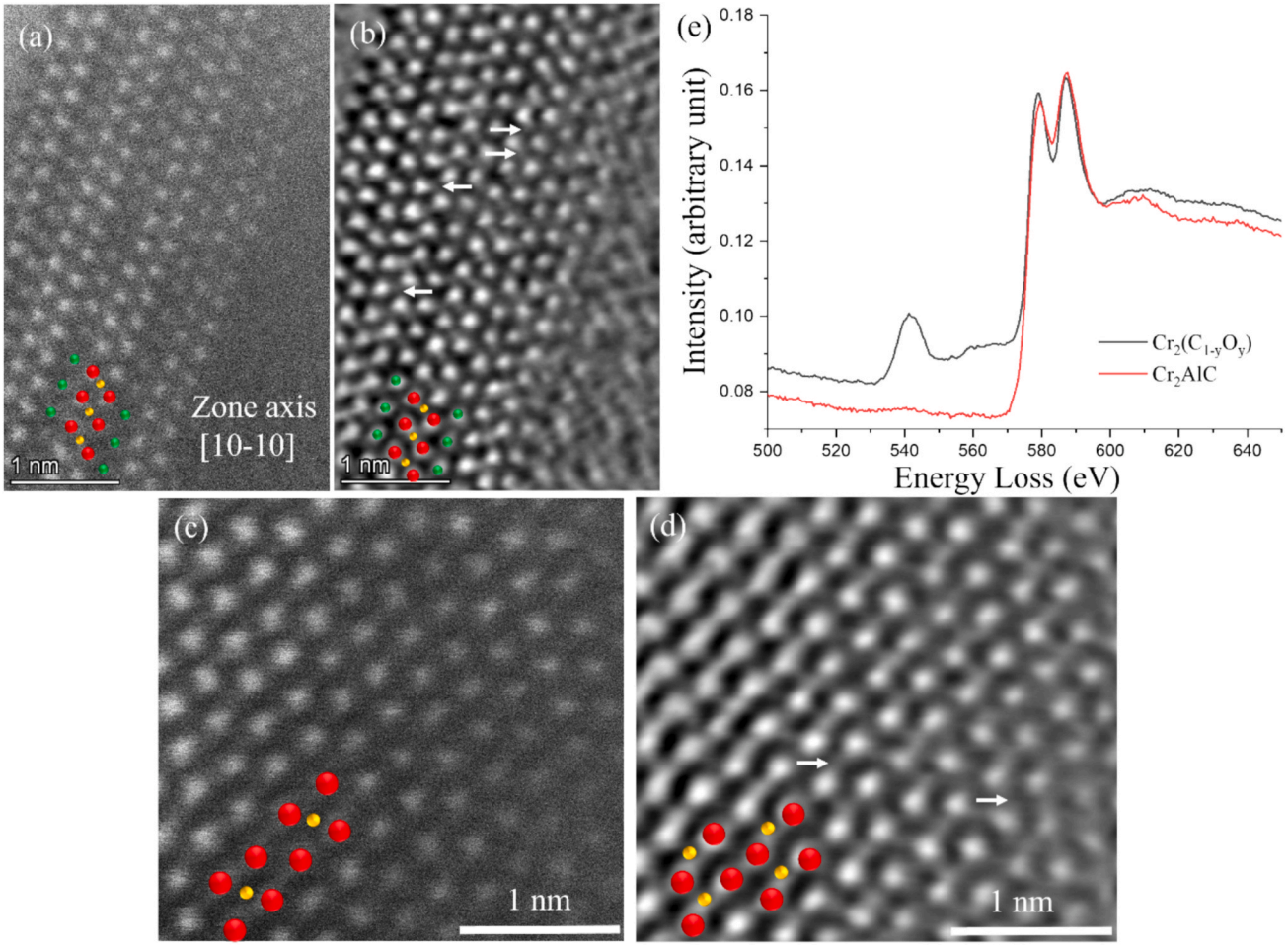

Fig. 4. Simultaneously acquired HAADF and iDPC STEM images of Cr_2AlC (a)-(b) and $Cr_2(C_{1-y}O_y)$ (c)-(d). Atomic arrangement of Cr, Al, and C in Cr_2AlC (b) and Cr and C in $Cr_2(C_{1-y}O_y)$ (d) are identified and marked in the iDPC STEM image. White arrows denote missing atomic columns of C in both Cr_2AlC and $Cr_2(C_{1-y}O_y)$ phases. (e) A comparison of EELS from Cr_2AlC and $Cr_2(C_{1-y}O_y)$ grains is shown in (e).

amorphous AlO_x phases has been revealed utilizing advanced STEM imaging techniques. The formation of both phases was attributed to the selective out-diffusion of Al from the Cr_2AlC MAX phase, facilitated by the incorporated oxygen. Thereby, the formation of 3D-$Cr_2(C_{1-y}O_y)$ is favoured over the formation of a 2D MXene, which is consistent with DFT predictions.

CRediT authorship contribution statement

Rajib Sahu: Writing – review & editing, Writing – original draft, Visualization, Project administration, Methodology, Investigation, Formal analysis, Data curation, Conceptualization. **Peter J. Pöllmann:** Writing – review & editing, Writing – original draft, Visualization, Methodology, Investigation, Formal analysis, Data curation, Conceptualization. **Dimitri Bogdanovski:** Methodology, Investigation, Formal analysis. **Clio Azina:** Writing – review & editing, Formal analysis. **Ganesh Kumar Nayak:** Writing – review & editing, Methodology, Investigation, Formal analysis, Data curation. **Jochen M. Schneider:** Writing – review & editing, Supervision, Resources, Funding acquisition, Conceptualization. **Christina Scheu:** Writing – review & editing, Supervision, Resources, Conceptualization.

Declaration of competing interest

The authors declare that they have no known competing financial interests or personal relationships that could have appeared to influence the work reported in this paper.

Acknowledgements

D. B. and J. M. S. thank the IT Center of RWTH Aachen University for the provision of computational resources and IT support via the Jülich-Aachen Research Alliance's (JARA) JARA0206 grant. J. M. S. acknowledges financial support from the MPG fellow program. The authors gratefully acknowledge the Ministry for Culture and Science of the State of North Rhine-Westphalia (MKW NRW) for supporting this work as part of the NHR funding. The authors gratefully acknowledge the computing time provided to them on the high-performance computer CLAIX at the NHR Center NHR4CES with project id p0020883.

Appendix A. Supplementary material

Supplementary data to this article can be found online at https://doi.org/10.1016/j.apsusc.2025.163590.

Data availability

Data will be made available on request.

References

[1] M. Ozkan, K.A.M. Quiros, J.M. Watkins, T.M. Nelson, N.D. Singh, M. Chowdhury, T. Namboodiri, K.R. Talluri, E. Yuan, Curbing pollutant CO_2 by using two-dimensional MXenes and MBenes, Chem 10 (2024) 1–41.

[2] T. Xu, Y. Wang, Z. Xiong, Y. Wang, Y. Zhaou, X. Li, A Rising 2D Star: Novel MBenes with Excellent Performance in Energy Conversion and Storage, Nano-Micro Lett., 15 (2023) 1–50.

[3] S. He, Q. Zhu, R.A. Soomro, B. Xu, MXene derivatives for energy storage applications, Sustainable Energy & Fuel 4 (2020) 4988.

[4] K.R.G. Lim, A.D. Handoko, S.K. Nemani, B. Wyatt, H.Y. Jiang, J. Tang, B. Anasori, Z.W. Seh, Rational Design of Two-Dimensional Transition Metal Carbide/Nitride (MXene) Hybrids and Nanocomposites for Catalytic Energy Storage and Conversion, ACS Nano 14 (9) (2020) 10834–10864.

[5] B. Anasori, M.R. Lukatskaya, Y. Gogotsi, 2D metal carbides and nitrides (MXenes) for energy storage, Nat. Rev. Mater., 2 (2017) 16098.

[6] X. Li, Z. Huang, C.E. Shuck, G. Liang, Y. Gogotsi, C. Zhi, MXene chemistry, electrochemistry and energy storage applications, Nat. Rev., 6 (2022) 389.

[7] L.T. Alameda, R.W. Lord, J.A. Barr, P. Moradifar, Z.P. Metzger, B.C. Steimle, C. F. Holder, N. Alem, S.B. Sinnott, R.E. Schaak, Multi-Step Topochemical Pathway to Metastable Mo_2AlB_2 and Related Two-Dimensional Nanosheet Heterostructures, J. Am. Chem. Soc., 141 (27) (2019) 10852–10861.

[8] C.E. Shuck, K. Ventura-Martinez, A. Goad, S. Uzun, M. Shekhirev, Y. Gogotsi, Safe Synthesis of MAX and MXene: Guidelines to Reduce Risk During Synthesis, ACS Chem. Health Saf., 28 (2021) 326–338.

[9] M. Naguib, V.N. Mochalin, M.W. Barsoum, Y. Gogotsi, 25th Anniversary Article: MXenes: A New Family of Two-Dimensional Materials, Adv. Mater., 26 (2014) 992–1005.

[10] J. Zhou, J. Palisaitis, J. Halim, M. Dahlqvist, Q. Tao, I. Persson, L. Hultman, P.O. Å. Persson, J. Rosen, Boridene: Two-dimensional Mo4/3B2-x with ordered metal vacancies obtained by chemical exfoliation, Science 373 (2021) 801–805.

[11] B. Zhang, J. Zhou, Z. Sun, MBenes: progress, challenges and future, J. Mater. Chem. A 10 (2022) 15865.

[12] J. Wozniak, A. Jastrzębska, A. Olszyna, Challenges and opportunities in tailoring MAX phases as a starting material for MXenes development, Mater. Technol., 37 (2022) 1639–1650.

[13] C. Lamiel, I. Hussain, J.H. Warner, K. Zhang, Beyond Ti-based MXenes: A review of emerging non-Ti based metal-MXene structure, properties, and applications, Mater. Today 63 (2023) 323–338.

[14] M.H. Tran, A.M. Malik, M. Dürrschnabel, A. Regoutz, P. Thakur, T.-L. Lee, D. Perera, L. Molina-Luna, K. Albe, J. Rohrer, C.S. Birkel, Experimental and theoretical investigation of the chemical exfoliation of Cr-based MAX phase particles, Dalton Trans., 49 (2020) 12215–12221.

[15] M.W. Barsoum, MAX phases: Properties of Machinable Ternary Carbides and Nitrides, John Wiley & Sons, 2013.

[16] C. Azina, J. Palisaitis, D. Bogdanovski, T. Bartsch, R. Sahu, C. Scheu, P. Persson, P. Eklund, J.M. Schneider, Formation of 3D Cr2C through solid state reaction-mediated Al extraction within Cr2AlC/Cu thin films, Nanoscale (2025), https://doi.org/10.1039/D4NR03664F.

[17] N.C. Frey, J. Wang, G.I.V. Bellido, B. Anasori, Y. Gogotsi, V.B. Shenoy, Prediction of Synthesis of 2D Metal Carbides and Nitrides (MXenes) and Their Precursors with Positive and Unlabeled Machine Learning, ACS Nano 13 (2019) 3031–3041.

[18] Y. Cheng, J. Dai, Y. Zhang, Y. Song, Transition metal modification and carbon vacancy promoted Cr_2CO_2 (MXenes): a new opportunity for a highly active catalyst for the hydrogen evolution reaction, J. Mater. Chem. A 6 (2018) 20956–20965.

[19] Y. Cheng, Y. Zhang, Y. Li, J. Dai, Y. Song, Hierarchical Ni_2P/Cr_2CT_x (MXene) composites with oxidized surface groups as efficient bifunctional electrocatalysts for overall water splitting, J. Mater. Chem. A 7 (2019) 9324–9334.

[20] Y. Cheng, L. Wang, Y. Li, Y. Song, Y. Zhang, The Etching, Exfoliation Properties of Cr $_2$AlC into Cr_2CO_2 and Electrocatalytic Performances of 2D Cr_2CO_2 MXene, J. Phys. Chem. C 123 (25) (2019) 15629–15636.

[21] Y. Cheng, J. Dai, Y. Song, Y. Zhang, Nanostructure of Cr_2CO_2 MXene supported single metal atom as an efficient bifunctional electrocatalyst for overall water splitting, ACS Appl. Energy Mater. 2 (9) (2019) 6851–6859.

[22] A. Yadav, Alpa Dashora b, N. Patel, A. Miotello, M. Press and D.C. Kothari, Study of 2D MXene Cr_2C material for hydrogen storage using density functional theory, Appl. Surf. Sci., 2016, 389, 88–95.

[23] D. Sun, Q. Hu, J. Chen, X. Zhang, L. Wang, Q. Wu, A. Zhou, Structural Transformation of MXene (V_2C, Cr_2C, and Ta_2C) with O Groups during Lithiation: A First-Principles Investigation, ACS Appl. Mater. Interfaces 8 (1) (2016) 74–81.

[24] Z. Xu, X. Lv, J. Chen, L. Jiang, Y. Laia, J. Li, DFT investigation of capacious, ultrafast and highly conductive hexagonal Cr_2C and V_2C monolayers as anode materials for high-performance lithium-ion batteries, Phys. Chem. Chem. Phys., 19 (2017) 7807–7819.

[25] F. Li, C.R. Cabrera, J. Wang, Z. Chen, A Cr_2CO_2 monolayer as a promising cathode for lithium and non-lithium ion batteries: a computational exploration, RSC Adv., 6 (2016) 81591–81596.

[26] R. Sahu, D. Bogdanovski, J.-O. Achenbach, S. Zhang, M. Hans, D. Primetzhofer, J. M. Schneider, C. Scheu, Direct MoB MBene domain formation in magnetron sputtered MoAlB thin films, Nanoscale 13 (2021) 18077–18083.

[27] R. Sahu, D. Bogdanovski, J.-O. Achenbach, M. Hans, D. Primetzhofer, J. M. Schneider, C. Scheu, Compositional defects in a MoAlB MAB phase thin film grown by high-power pulsed magnetron sputtering, Nanooscale 15 (2023) 17356–17363.

[28] J.-O. Achenbach, R. Sahu, B. Völker, M. Hans, D. Primetzhofer, D.J. Miljanovic, C. Scheu, J.M. Schneider, Synthesis and Properties of Orthorhombic MoAlB Coatings, Coatings 9 (2019) 510.

[29] R. Sahu, D. Bogdanovski, J.-O. Achenbach, J.M. Schneider, C. Scheu, Defects in an orthorhombic MoAlB MAB phase thin film grown at moderate synthesis temperature, Nanoscale 14 (2022) 2578–2585.

[30] J.C. Schuster, H. Nowotny, C. Vaccaro, The ternary systems: Cr-Al-C, V-Al-C and Ti-Al-C and the behavior of H-phases (M2AlC), J. Solid State Chem., 32 (1980) 213–219.

[31] G. Kresse, J. Furthmüller, Efficient iterative schemes for ab initio total-energy calculations using a plane-wave basis set, Phys. Rev. B: Condens. Matter Mater. Phys., 54 (1996) 11169–11186.

[32] G. Kresse, J. Furthmüller, Efficiency of *ab initio* total energy calculations for metals and semiconductors using a plane-wave basis set, Comput. Mater. Sci., 6 (1996) 15–20.

[33] J.P. Perdew, K. Burke, M. Ernzerhof, Generalized Gradient Approximation Made Simple, Phys. Rev. Lett., 77 (1997) 3865–3868.

[34] P.E. Blöchl, Projector augmented-wave method, Phys. Rev. B: Condens. Matter Mater. Phys., 50 (1994) 17953–17979.

[35] H.J. Monkhorst, J.D. Pack, Special points for Brillouin-zone integrations, Phys. Rev. B: Solid State 13 (1976) 5188–5198.

[36] M. Methfessel, A.T. Paxton, High-precision sampling for Brillouin-zone integration in metals, Phys. Rev. B: Condens. Matter Mater. Phys., 40 (1989) 3616–3621.

[37] M. Dahlqvist, B. Alling, J. Rosen, Correlation between magnetic state and bulk modulus of Cr2AlC, J. Appl. Phys., 113 (2013) 216103.

[38] S.J. Pennycook, P.D. Nellist, Scanning transmission electron microscopy, Springer, New York, 2011.

[39] B. Stelzer, X. Chen, P. Bliem, M. Hans, B. Völker, R. Sahu, C. Scheu, D. Primetzhofer, J.M. Schneider, Remote tracking of phase changes in Cr2AlC thin films by in-situ resistivity measurements, Sci. Rep., 9 (2019) 8266.

[40] J.M. Schneider, D.P. Sigumonrong, D. Music, C. Walter, J. Emmerlich, R. Iskandar, J. Mayer, Elastic properties of Cr_2AlC thin films probed by nanoindentation and ab initio molecular dynamics, Scr. Mater., 57 (2007) 1137–1140.

[41] B. Völker, B. Stelzer, S. Mráz, H. Rueß, R. Sahu, C. Kirchlechner, G. Dehm, J. M. Schneider, On the fracture behavior of Cr2AlC coatings, Mater. Des., 206 (2021) 109757.

[42] S.D. Findlay, N. Shibata, H. Sawada, E. Okunishi, Y. Kondo, Y. Ikuhara, Dynamics of annular bright field imaging in scanning transmission electron microscopy, Ultramicroscopy 110 (2010) 903–923.

[43] M. Baben, L. Shang, J. Emmerlich, J.M. Schneider, Oxygen incorporation in M_2AlC (M = Ti, V, Cr), Acta Mater., 60 (2012) 4810–4818.